Supporting Information for "Aerosol Effects on Clear-Sky Shortwave Heating in the Asian Monsoon Tropopause Layer"

Jie Gao[1], Yi Huang[2], Yiran Peng[1], and Jonathon S. Wright[1]

[1]Department of Earth System Science, Ministry of Education Key Laboratory for Earth System Modeling, and Institute for Global Change Studies, Tsinghua University, Beijing, China

[2]Department of Atmospheric and Oceanic Sciences, McGill University, Montreal, Quebec, Canada

Contents of this file

Introduction. This document summarizes technical details and previously published validation for MERRA-2 (Text S1; Table S1) and other reanalysis and forecast products (Text S2) as discussed in the main text. Nine supplementary figures are also included, mainly focusing on the species distributions in MERRA-2 and other products (Figs. S1–S5). Two alternative approaches to the calculation of ATAL radiative effects are also included (Figs. S6 and S7), along with two figures summarizing the magnitude of the ATAL effect relative to other factors as represented by MERRA-2 (Figs. S8 and S9).

Text S1: Additional details on MERRA-2. MERRA-2 is a state-of-the-art atmospheric reanalysis of the satellite era (1980–present) produced by the National Aeronautics and Space Administration (NASA) Global Modeling and Assimilation Office (GMAO). The model is run using version 5.12.4 of the Goddard Earth Observing System atmospheric model (GEOS-5) on a ∼50-km cubed sphere grid (data grid: 0.5°lat×0.625°lon) with 72 vertical levels and a model top at 0.01 hPa. The data assimilation takes place in two steps, with an incremental analysis update (Bloom et al., 1996) to apply adjustments calculated during an initial 3D-variational assimilation (additional details in Wright et al., 2022). Optical properties are largely taken from the Optical Properties of Aerosols and Clouds (OPAC) dataset (Hess et al., 1998) with some modifications. In particular, organic carbon from biomass burning is now partitioned directly to 'brown carbon' and dust optical properties are calculated assuming ellipsoid rather than spherical shapes (M. Chin, personal communication, 18 July 2020). With the exception of dust, aerosol hygroscopic growth is parameterized using separate functions of ambient relative humidity for each aerosol type (Chin et al., 2002; Colarco et al., 2014). Aerosol extinction coefficients increase with increasing relative humidity.

Aerosol data assimilation in MERRA-2 is restricted to measurements of vertically-integrated aerosol optical depth (AOD), and does not affect the composition and applies to all vertical levels simultaneously (Randles et al., 2017). Dust and sea salt emissions are wind-driven. Volcanic emissions are limited to an annually-repeating climatology of outgassing volcanoes, and do not account for volcanic eruptions that occurred after 2010. Anthropogenic aerosol emissions are taken from prescriptions developed for the AeroCom Phase II model intercomparison activity (Diehl et al., 2012), along with SO_2 from aircraft

and outgassing volcanoes. Emissions sources from AeroCom during our analyis period are fixed to values from 2006 (anthropogenic aerosols and aircraft SO_2) or 2007 (aerosol emissions from international shipping). Anthropogenic emissions of SO_2 from other sources are taken from the EDGARv4 database (Janssens-Maenhout, 2010, 2011). Emissions sources from EDGAR are fixed to values from 2005 (SO_2 from shipping; EDGARv4.1) or 2008 (anthropogenic SO_2; EDGARv4.2). Emissions of biogenic terpene are taken from the monthly climatology developed by Guenther et al. (1995), while emissions of dimethyl sulfide and methanesulfonic acid are taken from the monthly climatologies reported by Randerson et al. (2006).

Randles et al. (2017) evaluated the MERRA-2 aerosol analysis in terms of AOD and the aerosol direct radiative effects on clear-sky shortwave fluxes at the nominal top-of-atmosphere, surface, and net atmospheric convergence. Their results showed good agreement in both AOD and radiative effects validated against independent (i.e., unassimilated) measurements. Buchard et al. (2017) extended this validation to include aerosol absorption optical depth, ultraviolet aerosol index, and vertical aerosol profiles. Aerosol absorption optical depths and ultraviolet indices were in good agreement with values retrieved by the Ozone Monitoring Instrument (OMI), with evident improvement relative to aerosol analyses conducted using an earlier version of the GEOS-5 system (Buchard et al., 2015). Values of ultraviolet aerosol index tend to be biased low in areas with large values of brown carbon, which is not included in the MERRA-2 aerosol model and is also neglected in this study. MERRA-2 was also judged to perform well with respect to aerosol vertical profiles, although vertical gradients were often weaker than observed. Buchard et al. (2017) recommended that nearest-neighbor weighted combinations be used to improve

agreement with measured profiles. Since our analysis does not include direct comparison to measured profiles, we adopt a rough analogue to this approach by downgrading the spatial grid to 2.5°×2.5°, so that each profile is averaged across twenty grid cells (four in longitude by five in latitude).

Among available analysis and forecast products with an interactive ATAL (see section 4.2 in main text for examples), we choose to focus on MERRA-2 for two reasons. First, the MERRA-2 aerosol analysis is one of the few available aerosol analysis products to cover the entire period 2011–2020 using a consistent model and data assimilation system. This advantage in coverage provides a fuller characterization of the climatology and variability of the ATAL at interannual and intraseasonal scales, with the caveat that, as outlined above, most emissions sources do not vary from year to year during the 2011–2020 period. MERRA-2 for this period is thus not suitable for studying trends or variability linked to emissions (e.g., COVID-19), but is well suited to evaluating interannual variability driven by variations in the monsoon circulation and convective activity. Second, MERRA-2 is one of the few products to publish clear-sky radiative heating rate diagnostics along with interactive aerosol fields, which provide useful context for the offline radiative transfer calculations. These heating rates are calculated with reference to the aerosol fields during the incremental analysis update and are therefore consistent with ATAL composition and vertical structure as represented by the MERRA-2 products listed in Table S1.

Text S2: Other reanalysis products Several other recent reanalyses and operational forecasts of atmospheric composition are used to approximate uncertainty bounds for ATAL effects on clear-sky shortwave radiative heating (Table 2 in main text).

The first additional product, GEOS-FP (Forward Processing), is produced using a newer version of the same atmospheric model and data assimilation system as MERRA-2 (Lucchesi, 2018). Key developments relative to MERRA-2 include a finer horizontal model grid and the inclusion of nitrate and ammonium aerosols in the aerosol analysis. GEOS-FP uses the same emissions sources as MERRA-2: anthropogenic aerosol emissions and SO_2 from outgassing volcanoes are taken from the AeroCom Phase II archive (Diehl et al., 2012), while anthropogenic emissions of SO_2 and nitrate precursors from non-aircraft sources are taken from EDGARv4 (Janssens-Maenhout, 2010, 2011). We use the GEOS-FP analysis aerosol product on model levels for July–August 2020.

Two products from the Copernicus Atmosphere Monitoring Service (CAMS) and the European Centre for Medium-range Weather Forecasts (ECMWF) are considered, the CAMS ECMWF Atmospheric Composition Reanalysis 4 (CAMS-EAC4; Inness et al., 2019) for the full period 2011–2020 and the CAMS atmospheric composition forecast product (CAMS-FC; Rémy et al., 2019) for July–September 2020. Both CAMS-EAC4 and CAMS-FC use the Integrated Forecast System chemistry (IFS-CB05; Flemming et al., 2015) and aerosol (IFS-AER; Rémy et al., 2019) models. The CAMS-EAC4 product uses emissions from Monitoring Atmospheric Composition and Climate–CityZen (MACCity; Granier et al., 2011; Stein et al., 2014) for anthropogenic sources, Global Fire Assimilation System (GFAS) version 1.2 (Kaiser et al., 2012) for biomass burning, Model of Emissions of Gases and Aerosols from Nature (MEGAN) simulations for biogenic emissions (Sindelarova et al., 2014), and a climatology of volcanic outgassing. Unlike GEOS-FP and CAMS-EAC4, we use forecast rather than analysis products from CAMS-FC. CAMS-FC has a finer horizontal resolution and additional vertical levels relative to

CAMS-EAC4, includes nitrate and ammonium aerosols where CAMS-EAC4 does not, and implements a more realistic relationship between sulfur dioxide (from the chemistry scheme) and sulfate aerosols (from the aerosol scheme). Emissions sources are similar, but with version 1.2 of GFAS replaced by version 1.4. This and other differences between CAMS-EAC4 and CAMS-FC have been documented in detail by Rémy et al. (2019).

The final additional dataset is a set of 10-day forecast products generated by the National Center for Atmospheric Research (NCAR) Atmospheric Chemistry Observations & Modeling group using version 6 of the Whole Atmosphere Community Climate Model (WACCM; Gettelman et al., 2019). Interactive chemistry is based on the Model for OZone and Related chemical Tracers for the Troposphere, Stratosphere, Mesosphere, and Lower Thermosphere (MOZART-TSLMT; Emmons et al., 2020) and aerosols are simulated using the Modal Aerosol Module (MAM4; Liu et al., 2016; Tilmes et al., 2019). Anthropogenic emissions are the same as in the CAMS products (MACCity), while fire emissions are taken from the Fire INventory from NCAR (FINN; Wiedinmyer et al., 2011). Volcanic emissions are based on a time-mean climatology for 1850–2014 that includes both outgassing and eruptive emissions (Neely III & Schmidt, 2016). No observations are assimilated in the WACCM forecasts; however, the model is driven by meteorological fields taken from the GEOS-FP product described above. WACCM forecasts are used for July–September 2020.

Given data availability limitations and model version changes, the forecast and analysis products GEOS-FP, CAMS 46r1FC, and WACCM are used only for comparison with MERRA-2 during the year 2020 (section 4.2 in main text).

References

Bloom, S. C., Takacs, L. L., da Silva, A. M., & Ledvina, D. (1996). Data assimilation using incremental analysis updates. *Mon. Wea. Rev.*, *124*, 1256–1271. doi: 10.1175/1520-0493(1996)124⟨1256:DAUIAU⟩2.0.CO;2

Buchard, V., da Silva, A. M., Colarco, P. R., Darmenov, A., Randles, C. A., Govindaraju, R., ... Spurr, R. (2015). Using the OMI aerosol index and absorption aerosol optical depth to evaluate the NASA MERRA Aerosol Reanalysis. *Atmos. Chem. Phys.*, *15*(10), 5743–5760. doi: 10.5194/acp-15-5743-2015

Buchard, V., Randles, C. A., Silva, A. M. d., Darmenov, A., Colarco, P. R., Govindaraju, R., ... Yu, H. (2017). The MERRA-2 Aerosol Reanalysis, 1980 Onward. Part II: Evaluation and Case Studies. *J. Climate*, *30*(17), 6851–6872. doi: 10.1175/jcli-d-16-0613.1

Chin, M., Ginoux, P., Kinne, S., Torres, O., Holben, B. N., Duncan, B. N., ... Nakajima, T. (2002). Tropospheric aerosol optical thickness from the GOCART model and comparisons with satellite and sun photometer measurements. *J. Atmos. Sci.*, *59*, 461–483. doi: 10.1175/1520-0469(2002)059⟨0461:TAOTFT⟩2.0.CO;2

Colarco, P. R., Nowottnick, E. P., Randles, C. A., Yi, B., Yang, P., Kim, K.-M., ... Bardeen, C. G. (2014). Impact of radiatively interactive dust aerosols in the NASA GEOS-5 climate model: Sensitivity to dust particle shape and refractive index. *J. Geophys. Res. Atmos.*, *119*(2), 753–786. doi: 10.1002/2013jd020046

Diehl, T., Heil, A., Chin, M., Pan, X., Streets, D., Schultz, M., & Kinne, S. (2012). Anthropogenic, biomass burning, and volcanic emissions of black carbon, organic carbon, and SO_2 from 1980 to 2010 for hindcast model experiments. *Atmos. Chem.*

Phys. Discuss., *12*, 24895–24954. doi: 10.5194/acpd-12-24895-2012

Emmons, L. K., Schwantes, R. H., Orlando, J. J., Tyndall, G., Kinnison, D., Lamarque, J.-F., ... Pétron, G. (2020). The chemistry mechanism in the Community Earth System Model Version 2 (CESM2). *J. Adv. Model. Earth Syst.*, *12*(4), e2019MS001882. doi: 10.1029/2019MS001882

Flemming, J., Huijnen, V., Arteta, J., Bechtold, P., Beljaars, A., Blechschmidt, A.-M., ... Tsikerdekis, A. (2015). Tropospheric chemistry in the Integrated Forecasting System of ECMWF. *Geosci. Model Dev.*, *8*(4), 975–1003. Retrieved from `https://gmd.copernicus.org/articles/8/975/2015/` doi: 10.5194/gmd-8-975-2015

Gettelman, A., Mills, M. J., Kinnison, D. E., Garcia, R. R., Smith, A. K., Marsh, D. R., ... Randel, W. J. (2019). The Whole Atmosphere Community Climate Model Version 6 (WACCM6). *J. Geophys. Res. Atmos.*, *124*(23), 12380–12403. doi: 10.1029/2019JD030943

Global Modeling and Assimilation Office. (2015a). *MERRA-2 inst3_3d_aer_Nv: 3d, 3-Hourly, Instantaneous, Model-Level, ssimilation, Aerosol Mixing Ratio V5.12.4* [dataset]. NASA Goddard Earth Sciences Data and Information Services Center. doi: 10.5067/LTVB4GPCOTK2

Global Modeling and Assimilation Office. (2015b). *MERRA-2 inst3_3d_asm_Nv: 3d, 3-Hourly, Instantaneous, Model-Level, Assimilation, Assimilated Meteorological Fields V5.12.4* [dataset]. NASA Goddard Earth Sciences Data and Information Services Center. doi: 10.5067/WWQSXQ8IVFW8

Global Modeling and Assimilation Office. (2015c). *MERRA-2 tavg1_2d_rad_Nx: 2d, 1-Hourly, Time-Averaged, Single-Level, Assimilation, Radiation Diagnostics V5.12.4*

[dataset]. NASA Goddard Earth Sciences Data and Information Services Center. doi: 10.5067/Q9QMY5PBNV1T

Global Modeling and Assimilation Office. (2015d). *MERRA-2 tavg3_3d_rad_Nv: 3d, 3-Hourly, Time-Averaged, Model-Level, Assimilation, Radiation Diagnostics V5.12.4* [dataset]. NASA Goddard Earth Sciences Data and Information Services Center. doi: 10.5067/7GFQKO1T43RW

Granier, C., Bessagnet, B., Bond, T., D'Angiola, A., Gon, H. D. v. d., Frost, G. J., ... Vuuren, D. P. v. (2011). Evolution of anthropogenic and biomass burning emissions of air pollutants at global and regional scales during the 1980–2010 period. *Clim. Change*, *109*(1-2), 163. doi: 10.1007/s10584-011-0154-1

Guenther, A., Hewitt, C. N., Erickson, D., Fall, R., Geron, C., Graedel, T., ... Zimmerman, P. (1995). A global model of natural volatile organic compound emissions. *J. Geophys. Res. Atmos.*, *100*(D5), 8873–8892. doi: 10.1029/94JD02950

Hess, M., Koepke, P., & Schult, I. (1998). Optical Properties of Aerosols and Clouds: The software package OPAC. *Bull. Am. Meteor. Soc.*, *79*, 831–844. doi: 10.1175/1520-0477(1998)079⟨0831:opoaac⟩2.0.co;2

Inness, A., Ades, M., Agustí-Panareda, A., Barré, J., Benedictow, A., Blechschmidt, A.-M., ... Suttie, M. (2019). The CAMS reanalysis of atmospheric composition. *Atmos. Chem. Phys.*, *19*(6), 3515–3556. doi: 10.5194/acp-19-3515-2019

Janssens-Maenhout, G. (2010). *EDGARv4.1 Emission Maps* [dataset]. European Commission, Joint Research Centre (JRC). (http://data.europa.eu/89h/jrc-edgar-emissionmapsv41)

Janssens-Maenhout, G. (2011). *EDGARv4.2 Emission Maps* [dataset]. European

Commission, Joint Research Centre (JRC). (http://data.europa.eu/89h/jrc-edgar-emissionmapsv42)

Kaiser, J. W., Heil, A., Andreae, M. O., Benedetti, A., Chubarova, N., Jones, L., ... van der Werf, G. R. (2012). Biomass burning emissions estimated with a global fire assimilation system based on observed fire radiative power. *Biogeosciences*, *9*(1), 527–554. doi: 10.5194/bg-9-527-2012

Liu, X., Ma, P.-L., Wang, H., Tilmes, S., Singh, B., Easter, R. C., ... Rasch, P. J. (2016). Description and evaluation of a new four-mode version of the Modal Aerosol Module (MAM4) within version 5.3 of the Community Atmosphere Model. *Geosci. Model Dev.*, *9*(2), 505–522. doi: 10.5194/gmd-9-505-2016

Lucchesi, R. (2018). *File specification for GEOS-5 FP.* GMAO Office Note No. 4 (version 1.2), Greenbelt, Maryland. (62 pp., available at http://gmao.gsfc.nasa.gov/pubs/office_notes)

Neely III, R., & Schmidt, A. (2016). *Volcaneesm: Global volcanic sulphur dioxide (so2) emissions database from 1850 to present - version 1.0* [dataset]. NERC Centre for Environmental Data Analysis (CEDA). Retrieved from `https://catalogue.ceda.ac.uk/uuid/a8a7e52b299a46c9b09d8e56b283d385` doi: 10.5285/76EBDC0B-0EED-4F70-B89E-55E606BCD568

Randerson, J. T., Liu, H., Flanner, M. G., Chambers, S. D., Jin, Y., Hess, P. G., ... Zender, C. S. (2006). The impact of boreal forest fire on climate warming. *Science*, *314*(5802), 1130–1132. doi: 10.1126/science.1132075

Randles, C. A., Silva, A. M. d., Buchard, V., Colarco, P. R., Darmenov, A., Govindaraju, R., ... Flynn, C. J. (2017). The MERRA-2 Aerosol Reanalysis, 1980 onward. Part

I: System description and data assimilation evaluation. *J. Climate*, *30*, 6823–6850. doi: 10.1175/jcli-d-16-0609.1

Rémy, S., Kipling, Z., Flemming, J., Boucher, O., Nabat, P., Michou, M., ... Morcrette, J.-J. (2019). Description and evaluation of the tropospheric aerosol scheme in the European Centre for Medium-Range Weather Forecasts (ECMWF) Integrated Forecasting System (IFS-AER, cycle 45R1). *Geosci. Model Dev.*, *12*(11), 4627–4659. doi: 10.5194/gmd-12-4627-2019

Sindelarova, K., Granier, C., Bouarar, I., Guenther, A., Tilmes, S., Stavrakou, T., ... Knorr, W. (2014). Global data set of biogenic VOC emissions calculated by the MEGAN model over the last 30 years. *Atmos. Chem. Phys.*, *14*(17), 9317–9341. doi: 10.5194/acp-14-9317-2014

Stein, O., Schultz, M. G., Bouarar, I., Clark, H., Huijnen, V., Gaudel, A., ... Clerbaux, C. (2014). On the wintertime low bias of northern hemisphere carbon monoxide found in global model simulations. *Atmos. Chem. Phys.*, *14*(17), 9295–9316. doi: 10.5194/acp-14-9295-2014

Tilmes, S., Hodzic, A., Emmons, L. K., Mills, M. J., Gettelman, A., Kinnison, D. E., ... Liu, X. (2019). Climate forcing and trends of organic aerosols in the Community Earth System Model (CESM2). *J. Adv. Model. Earth Syst.*, *11*(12), 4323–4351. doi: https://doi.org/10.1029/2019MS001827

Wiedinmyer, C., Akagi, S. K., Yokelson, R. J., Emmons, L. K., Al-Saadi, J. A., Orlando, J. J., & Soja, A. J. (2011). The Fire INventory from NCAR (FINN): a high resolution global model to estimate the emissions from open burning. *Geosci. Model Dev.*, *4*(3), 625–641. Retrieved from `https://gmd.copernicus.org/articles/4/625/`

2011/ doi: 10.5194/gmd-4-625-2011

Wright, J. S., Fujiwara, M., Long, C., Anstey, J., Chabrillat, S., Compo, G. P., ... Zou, C.-Z. (2022). Chapter 2: Description of the Reanalysis Systems. In M. Fujiwara, G. Manney, L. Gray, & J. S. Wright (Eds.), *SPARC Report No. 10, WCRP Report 6/2021* (pp. 15–80). Munich: SPARC. doi: 10.17874/800DEE57D13

Table S1. MERRA-2 data collections used in this work.

Name	Variables	Time	Citation
M2I3NVAER	BC, OC, SO_4, dust	daily	Global Modeling and Assimilation Office (2015a)
M2I3NVASM	T, q, O_3, z, p	daily	Global Modeling and Assimilation Office (2015b)
M2T3NVRAD	SWHR, SWHRCLR	daily, 06Z	Global Modeling and Assimilation Office (2015d)
M2T1NXRAD	surface albedo	hourly	Global Modeling and Assimilation Office (2015c)

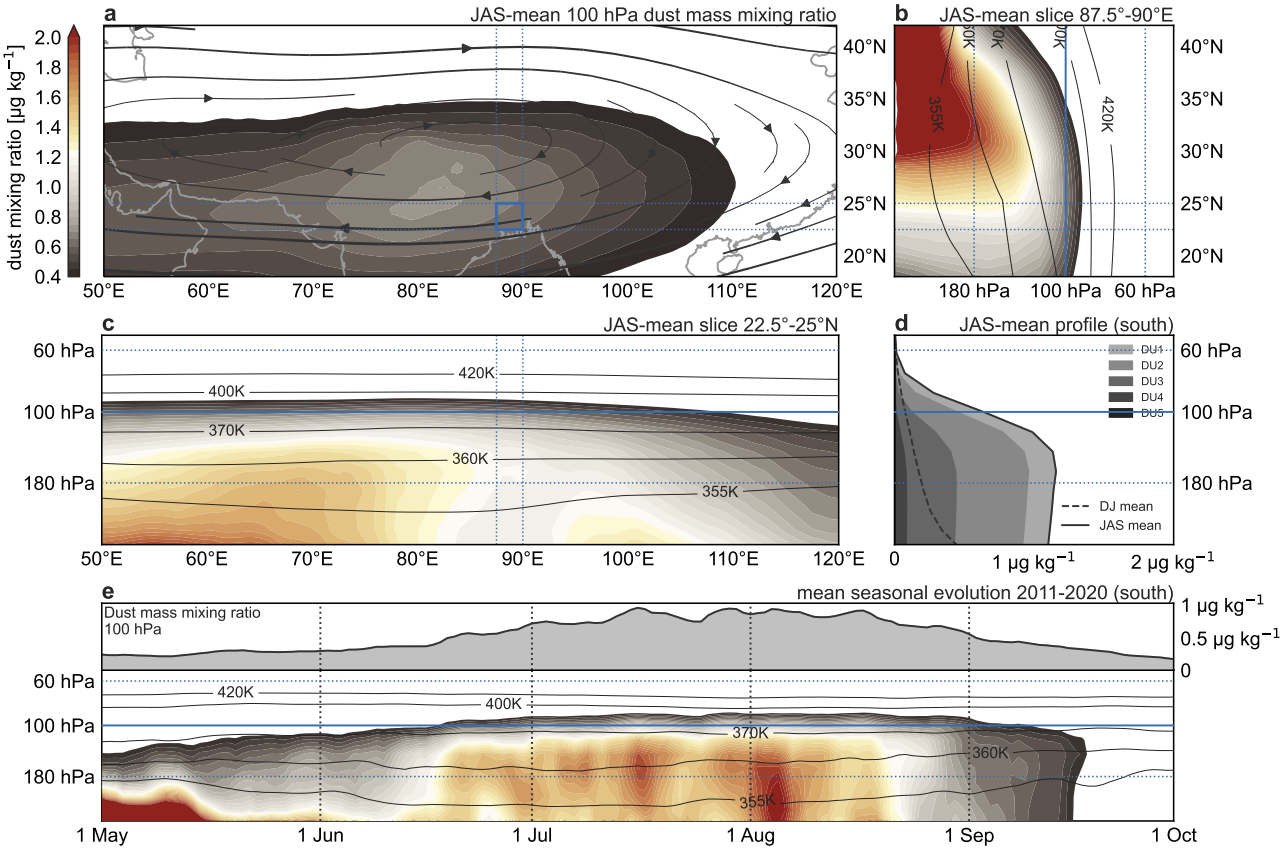

Figure S1. Distributions of mineral dust mass mixing ratios based on the MERRA-2 aerosol reanalysis (a) as a function of latitude and longitude on the 100 hPa isobaric surface, (b) as a function of latitude and pressure along the 87.5°E–90°E longitude band, (c) as a function of longitude and pressure along the 22.5°N–25°N latitude band, and (d) as an area-average profile within 87.5°E–90°E and 22.5°N–25°N for July, August, and September 2011–2020. (e) Mean evolution of dust profile (lower panel) and partial column (vertically-integrated over 180–60 hPa; upper panel) within 87.5°E–90°E and 22.5°N–25°N from 1 May to 30 September 2011–2020. Streamlines in (a) show the upper-level anticyclone at 100 hPa based on MERRA-2. Contours in (b), (c), and (e) show potential temperature surfaces spanning the upper troposphere and lower stratosphere. Shaded regions in (d) and (e) illustrate the relative abundances of different size bins of dust, listed from small (DU1, < 1 μm) to large (DU5; 6–10 μm).

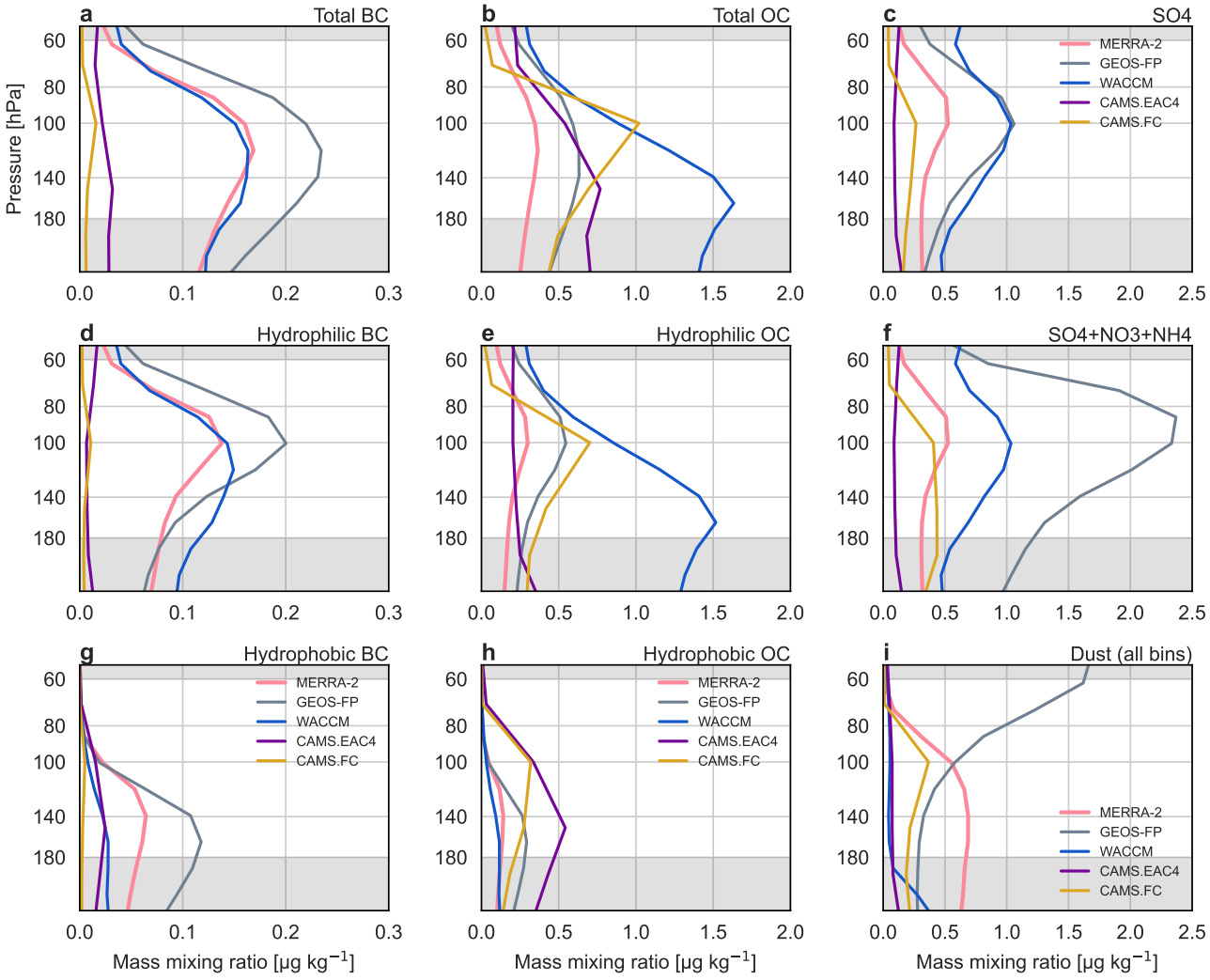

Figure S2. Vertical profiles of (a) total black carbon, (b) total organic carbon, (c) sulfate aerosol, (d) hydrophilic black carbon, (e) hydrophilic organic carbon, (f) sulfate + nitrate + ammonium aerosol, (g) hydrophobic black carbon, (h) hydrophobic organic carbon, and (i) mineral dust from all size bins based on the MERRA-2 (pink), GEOS-FP (grey), WACCM (blue), CAMS-EAC4 (purple), CAMS-FC (yellow) aerosol analysis (MERRA-2, GEOS-FP, and CAMS-EAC4) and forecast (WACCM and CAMS-FC) products. Grey shading indicates the bounds of the ATAL layer (60–180 hPa).

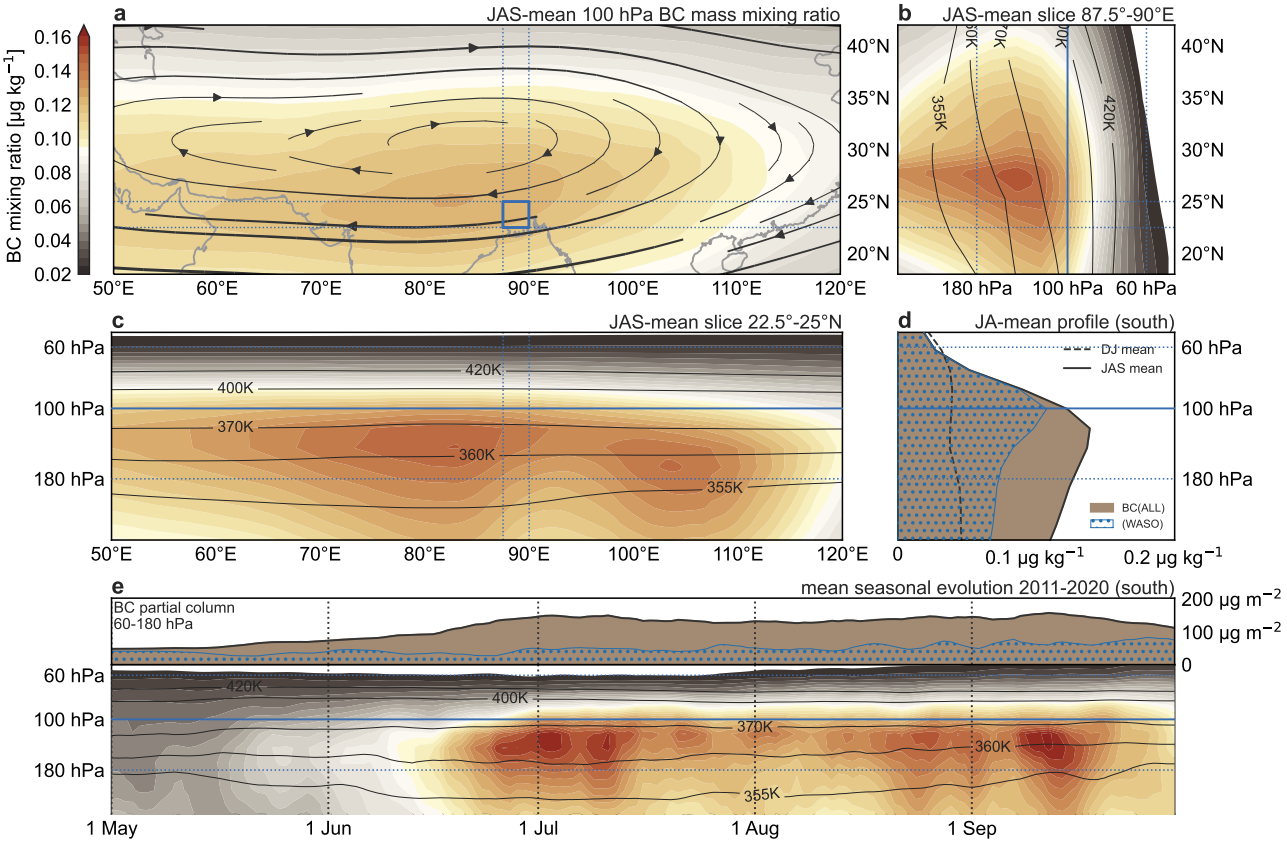

Figure S3. As in Fig. S1, but for black carbon (BC).

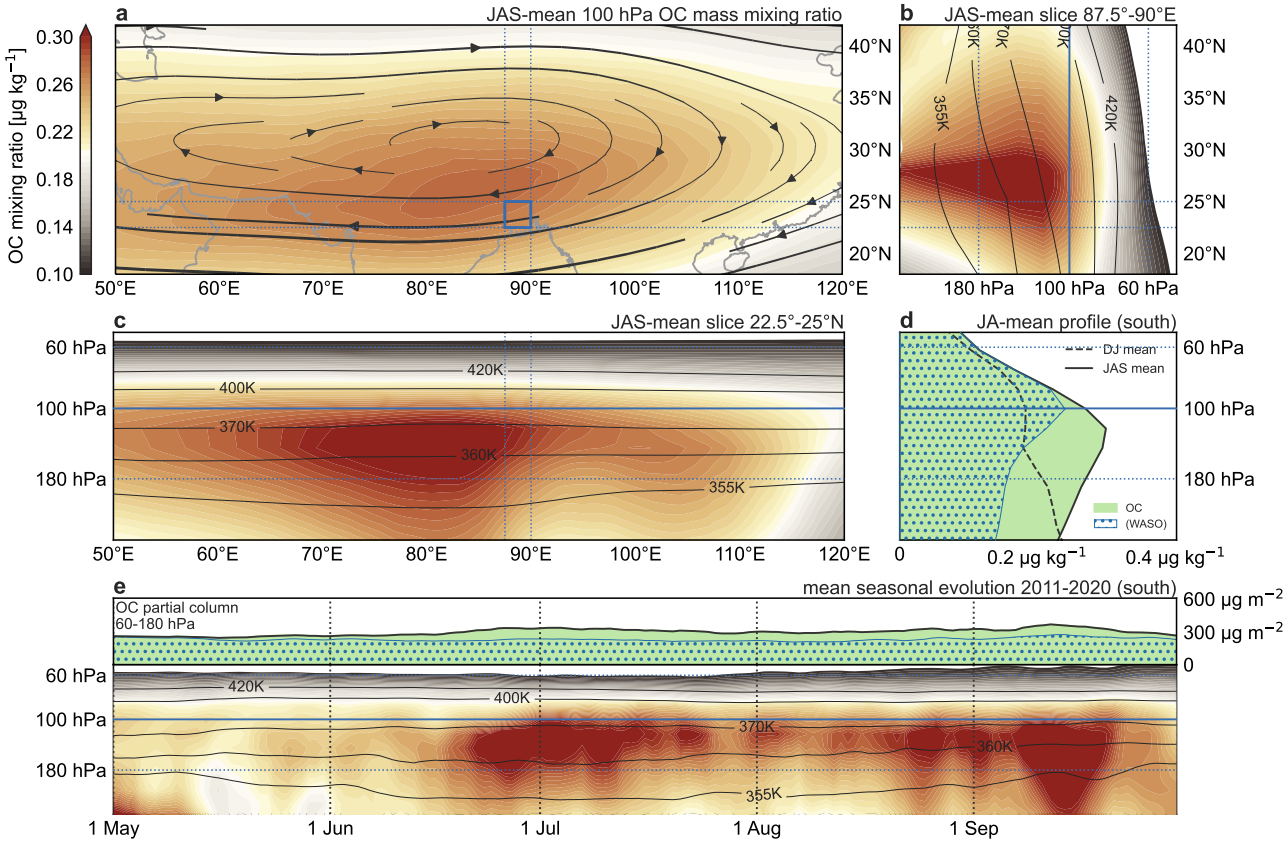

Figure S4. As in Fig. S1, but for organic carbon (OC).

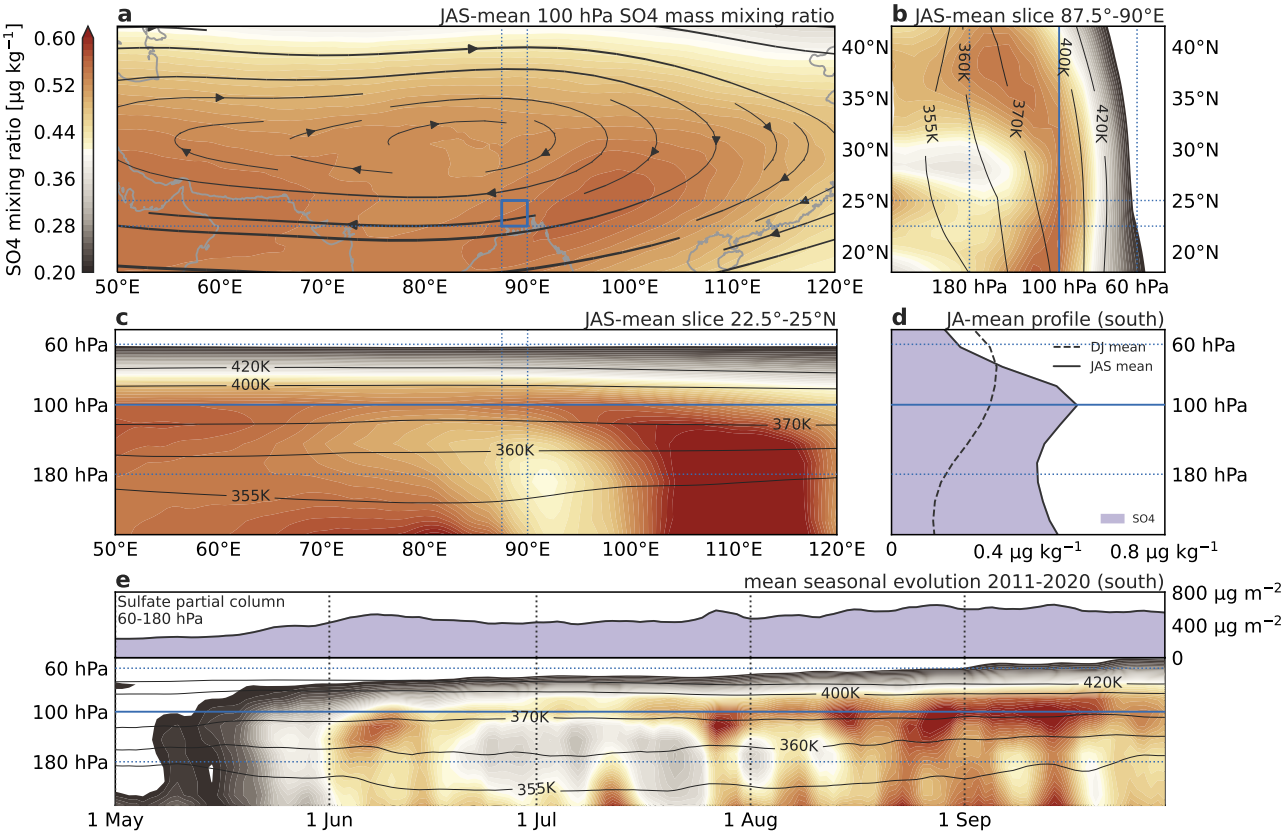

Figure S5. As in Fig. S1, but for sulfate.

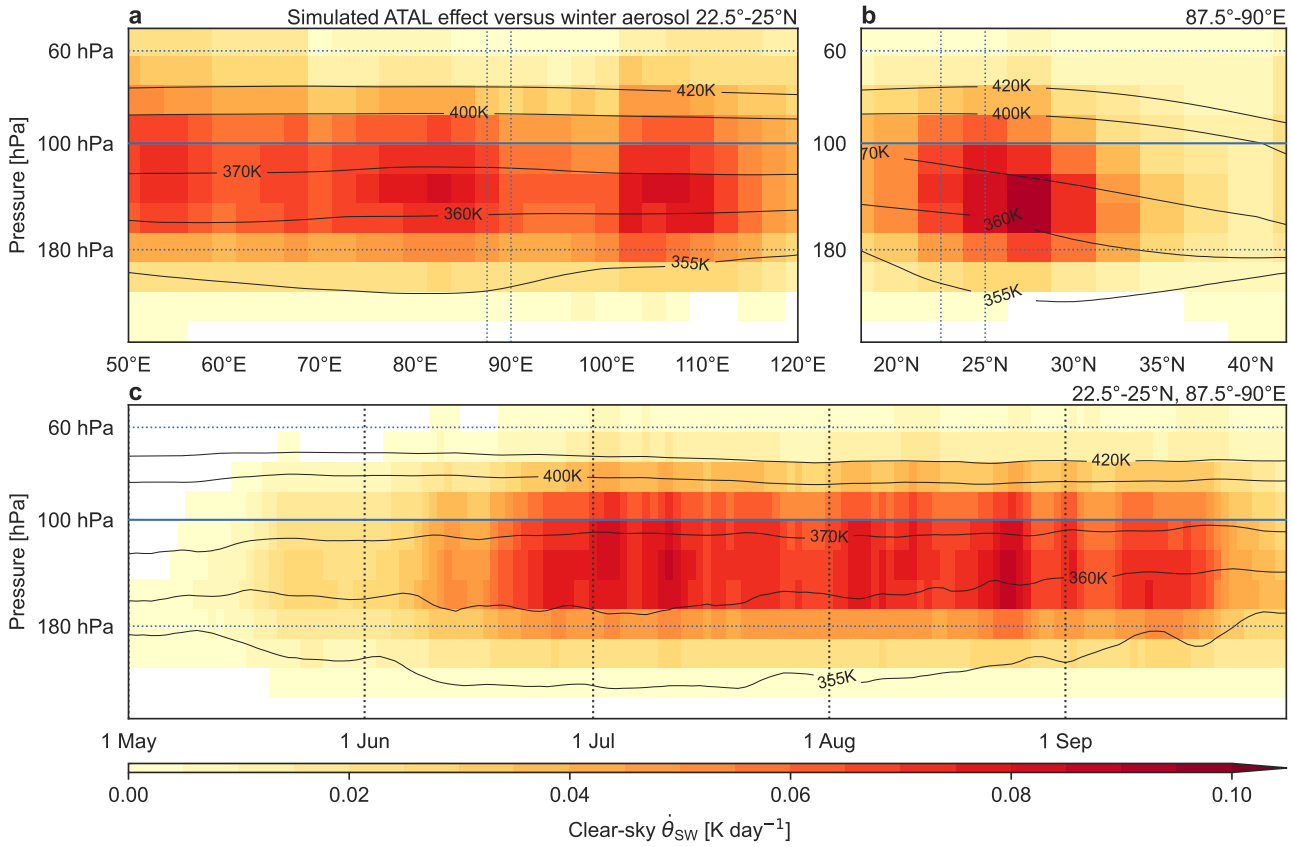

Figure S6. Variations in (a) longitude, (b) latitude, and (c) day-of-year for the simulated ATAL effect relative to an invariant representative winter-mean (December 2007 –January 2008) aerosol profile from MERRA-2 for the core region (22.5°N–25°N, 87.5°E–90°N). Panel c corresponds to Fig. 4b in the main text but with the winter-mean profile used as the reference state in place of the no-aerosol profile. Other radiatively active species are specified for both the winter-mean and ATAL simulations as July–August 2011–2020 means for each location in panels a–b and for each day of year averaged over 2011–2020 in the core region in panel c. Heating rates have been divided by the Exner function to convert $\partial T/\partial t$ to $\dot{\theta}$ for ease of comparison to potential temperature contours.

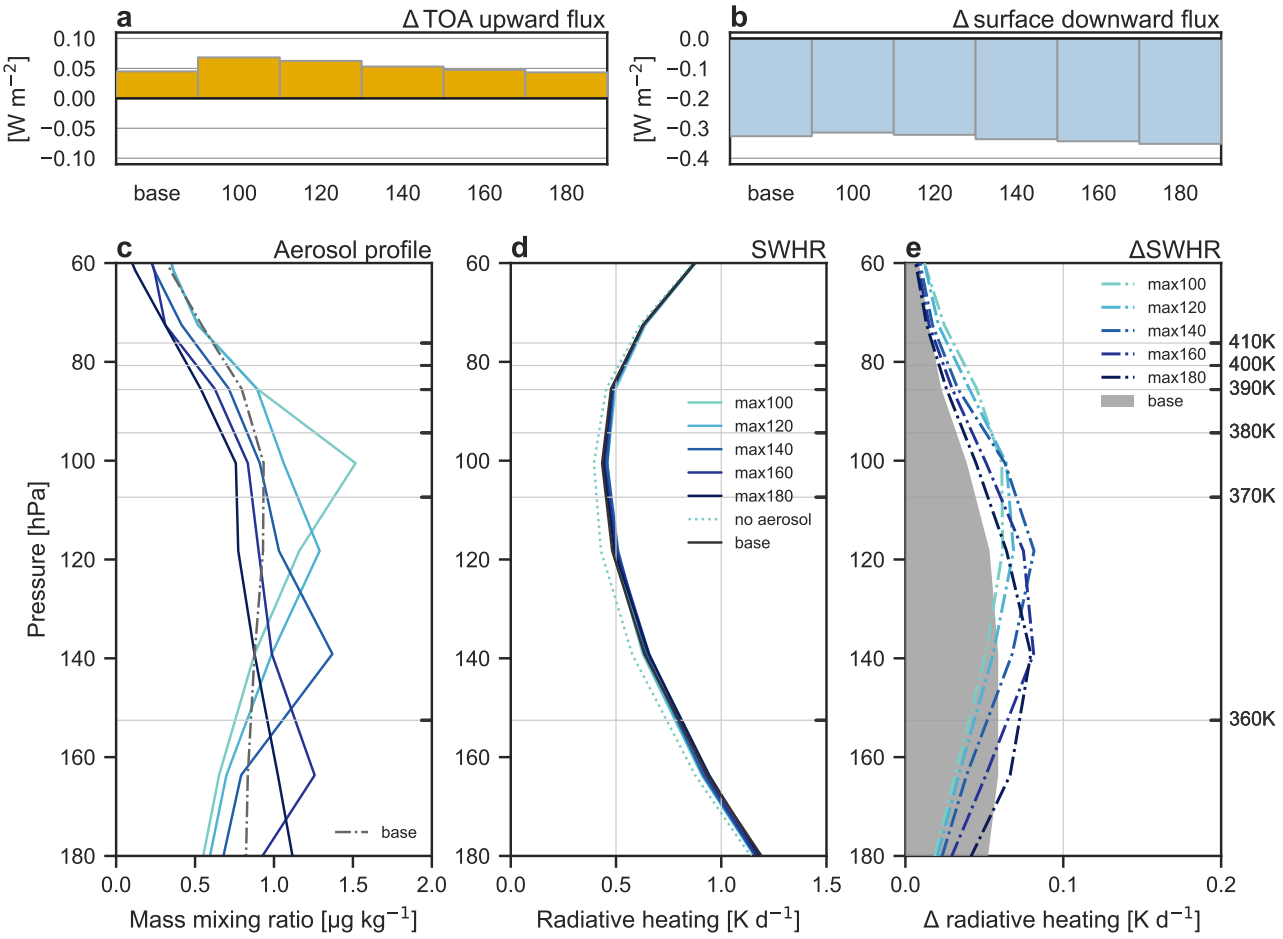

Figure S7. Variations in (a) top-of-atmosphere upward shortwave flux anomalies, (b) surface downward shortwave flux anomalies, (c) vertical profiles of aerosol mass mixing ratio, (d) shortwave radiative heating, and (e) aerosol effects on shortwave radiative heating relative to the no-aerosol case as a function of the height of the peak ATAL aerosol concentration. The vertically integrated mass and composition of ATAL aerosol are held fixed in all simulations while peak heights are varied from 100 hPa to 180 hPa. Heating rate profiles are calculated assuming a solar zenith angle of zero and a surface albedo of 0.15; TOA and surface fluxes are daily-mean values for solar parameters valid on 15 August at Dhaka.

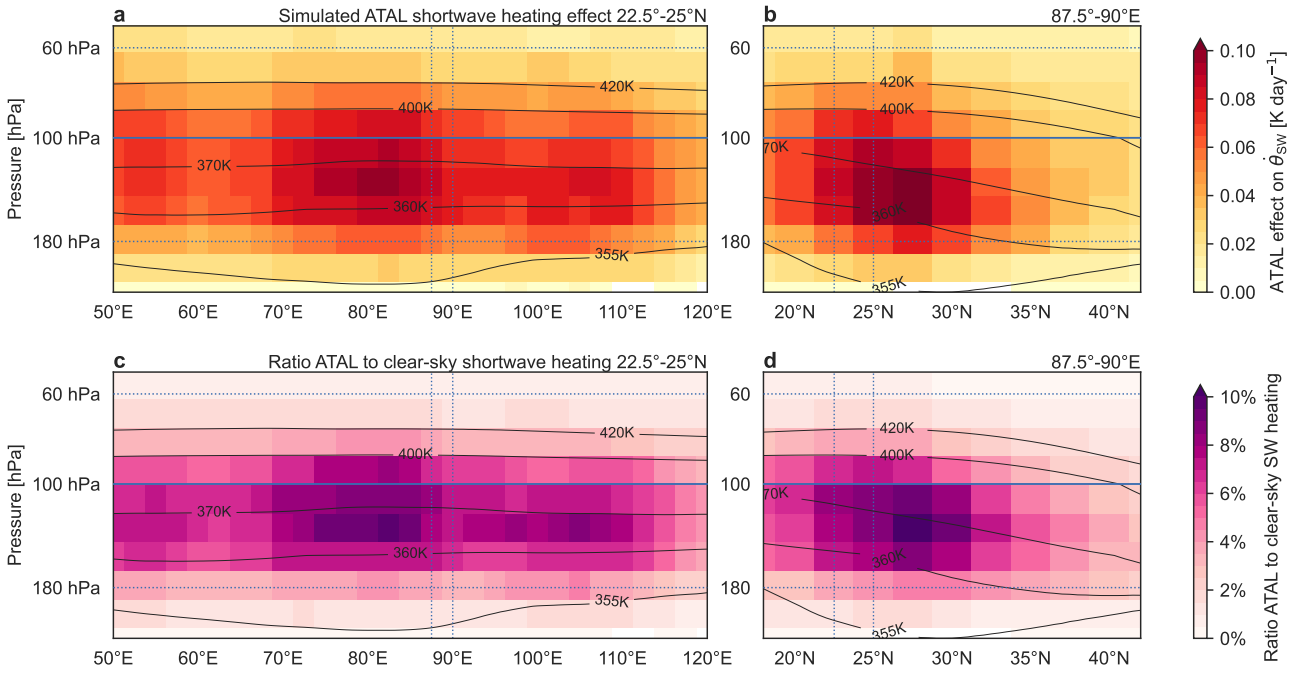

Figure S8. The mean ATAL shortwave heating effect as a function of (a) longitude (50°E–120°E meridionally averaged over 22.5°N–25°N) and latitude (18°N–42°N zonally averaged over 87.5°E–90°E). Lower panels show the ratio of the ATAL effects relative to (c)–(d) clear-sky shortwave heating from libRadtran. Inputs to libRadtran are based on July–September 2011–2020 means assuming a solar zenith angle of 0° and a surface albedo of 0.15. Heating rates in panels a–b have been divided by the Exner function to convert $\partial T/\partial t$ to $\dot{\theta}$ for ease of comparison to potential temperature contours.

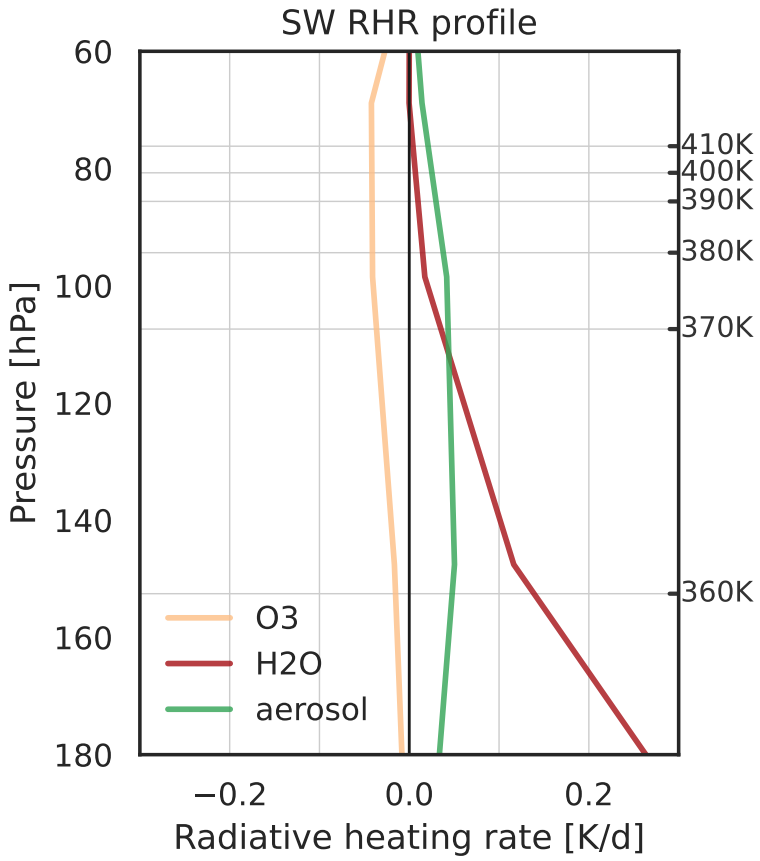

Figure S9. Vertical profiles of effects on clear-sky shortwave heating from ozone (yellow), water vapor (magenta), and aerosol (green) based on the July–August 2011–2020 mean for the core analysis region (22.5°N–25°N, 87.5°E–90°E) in MERRA-2. All effects are calculated by offline radiative transfer calculations assuming a solar zenith angle of 0° and a surface albedo of 0.15. The aerosol effect is calculated relative to the no-aerosol baseline; the ozone and water vapor effects are calculated for monsoon anomalies relative to zonal means within the 22.5°N–25°N latitude band. Heating rates are given as temperature tendency ($\partial T/\partial t$).